



# A simple variant selection in stress-driven martensitic transformation

HPSTAR  
787-2019

Binbin Yue<sup>a,b,c,1</sup>, Fang Hong<sup>a,b,1</sup>, Nahisa Hirao<sup>d</sup>, Roman Vasin<sup>e</sup>, Hans-Rudolf Wenk<sup>c,2</sup>, Bin Chen<sup>a,2</sup>, and Ho-Kwang Mao<sup>a,2</sup>

<sup>a</sup>Center for High Pressure Science and Technology Advanced Research, Pudong, 201203 Shanghai, People's Republic of China; <sup>b</sup>The Advanced Light Source, Lawrence Berkeley National Laboratory, Berkeley, CA 94720; <sup>c</sup>Department of Earth and Planetary Science, University of California, Berkeley, CA 94720; <sup>d</sup>SPRING-8, Japan Synchrotron Radiation Research Institute, Sayo-gun, 679-5198 Hyogo, Japan; and <sup>e</sup>Frank Laboratory of Neutron Physics, Joint Institute for Nuclear Research, 141980 Dubna, Russia

Contributed by Ho-Kwang Mao, May 20, 2019 (sent for review April 16, 2019; reviewed by Sergio Speziale and Quentin Williams)

The study of orientation variant selection helps to reveal the mechanism and dynamic process of martensitic transformations driven by temperature or pressure/stress. This is challenging due to the multiple variants which may coexist. While effects of temperature and microstructure in many martensitic transformations have been studied in detail, effects of stress and pressure are much less understood. Here, an in situ variant selection study of Mn<sub>2</sub>O<sub>3</sub> across the cubic-to-orthorhombic martensitic transformation explores orientation variants at pressures up to 51.5 GPa and stresses up to 5.5 GPa, using diamond anvil cells in radial geometry with synchrotron X-ray diffraction. The diamonds not only exert pressure but also impose stress and cause plastic deformation and texture development. The crystal orientation changes were followed in situ and a {110}<sub>c</sub> <001><sub>c</sub> // (100)<sub>o</sub> <010><sub>o</sub> relationship was observed. Only the {110}<sub>c</sub> plane perpendicular to the stress direction was selected to become (100)<sub>o</sub>, resulting in a very strong texture of the orthorhombic phase. Contrary to most other martensitic transformations, this study reveals a clear and simple variant selection that is attributed to structural distortions under pressure and stress.

martensitic transformations | variant selection | high pressure | oxide | radial diffraction

Martensitic transformations (MTs), solid to solid phase transitions characterized by a change of crystal structure resulting from diffusionless motion of atoms, have been known for more than a century (1–3). They are associated with changes in mechanical, transport, and electromagnetic properties that accompany the structure change (4–8). MTs have been found in various material systems and are the basic principle for shape memory and superelastic effects (9–12). They can be induced by either changes in temperature or pressure/stress (13), such as temperature-induced MTs in steel from body-centered cubic (bcc) ( $\alpha$ ) to face-centered cubic (fcc) ( $\gamma$ ) for which orientation relationships  $\{110\}_{\alpha} // \{111\}_{\gamma}$ ,  $(110)_{\alpha} // (112)_{\gamma}$  (14), and  $\{110\}_{\alpha} // \{111\}_{\gamma}$ ,  $\langle 111 \rangle_{\alpha} // \langle 110 \rangle_{\gamma}$  (15) have been proposed. In temperature-induced MTs from hexagonal close packed (hcp) ( $\alpha$ ) to bcc ( $\beta$ ) in zirconium, orientation relationships  $\{0001\}_{\alpha} // \{011\}_{\beta}$ ,  $\langle 11-20 \rangle_{\alpha} // \langle 111 \rangle_{\beta}$  have been proposed (16). In polycrystalline aggregates such transitions result in characteristic texture changes (17).

However, among all of the possible variants based on crystal symmetry, some may be favored during MTs due to microstructures, lattice strains, and imposed external stress or strain (18, 19). As a consequence, the transformed texture may differ significantly from the texture predicted by ideal orientation relationships. High-pressure experiments on zirconium confirmed the  $(0001)_{\alpha} // (11-20)_{\omega}$  relationship during its  $\alpha \rightarrow \omega$  MT transition and a remarkable orientation memory when  $\omega$  reverts back to  $\alpha$  (20). During the bcc ( $\alpha$ ) to hcp ( $\epsilon$ ) transition of iron under high pressure, a subset of orientations is favored to transform to hcp first and generate a texture different from the Burgers relationship (21, 22). When transformed from the high-temperature  $\gamma$  phase (fcc), the texture of  $\epsilon$  iron is also suggested to be subject to variant selection (23). It

was suggested that across the cubic–rhombohedral transition in wüstite, variant selection aligned  $\{11-20\}_r$  and  $\{10-11\}_r$  daughters of  $\{101\}_c$  and  $\{111\}_c$ , respectively, more closely perpendicular to the compression direction (24). Experiments on NaNiF<sub>3</sub>, an analog for high-pressure MgSiO<sub>3</sub>, showed that the perovskite to postperovskite transition in the D'' layer of the Earth's deep mantle may also be martensitic (25). However, in all these studies the variant selection was not characterized. For stress-induced tetragonal to monoclinic (T  $\rightarrow$  M) MTs in zirconia (ZrO<sub>2</sub>), Zeng et al. found that uniaxial stress preferred correspondence C (tetragonal  $c$  axis becomes the monoclinic  $c$  axis) (26, 27), while phase-field modeling showed that external stress favored the production of monoclinic variants which exhibit transformation strains aligned with the applied stress direction (28, 29). Compared with temperature-driven MTs, effects of stress and pressure are still much less understood. Hence, it is of great interest to study the variant selection effect in pressure/stress-driven MTs, which are important for both multifunctional material design and geodynamics.

Here, we chose Mn<sub>2</sub>O<sub>3</sub> as a model material to study the variant selection during the pressure-driven cubic–orthorhombic transition by using radial diamond anvil cell X-ray diffraction (r-DAC XRD), which imposes stress in addition to pressure

## Significance

Variant selection plays an important role during martensitic transformations in both metals and oxides. Due to its great effects on the crystallographic texture, it has received a great deal of attention in fields of physics, material science, and even Earth science. Previously, most studies focused on transitions in metals induced by temperature. Here, we investigate more complex oxides structures during the pressure/stress-driven martensitic transformation and find a very simple variant selection in cubic/orthorhombic Mn<sub>2</sub>O<sub>3</sub>. The high-pressure orthorhombic phase inherits texture from the low-pressure cubic phase. Only one of the six cubic {110} planes becomes the orthorhombic (100) plane: the one perpendicular to the compression direction. This will become a reference to demonstrate the variant selection behavior under high pressure.

Author contributions: B.Y., F.H., H.-R.W., B.C., and H.-K.M. designed research; B.Y., F.H., N.H., and R.V. performed research; B.Y., F.H., R.V., and H.-R.W. analyzed data; and B.Y., F.H., R.V., H.-R.W., B.C., and H.-K.M. wrote the paper.

Reviewers: S.S., GFZ German Research Centre for Geosciences, Helmholtz Centre Potsdam; and Q.W., University of California, Santa Cruz.

The authors declare no conflict of interest.

Published under the PNAS license.

<sup>1</sup>B.Y. and F.H. contributed equally to this work.

<sup>2</sup>To whom correspondence may be addressed. Email: wenk@berkeley.edu, chenbin@hpstar.ac.cn, or maohk@hpstar.ac.cn.

This article contains supporting information online at [www.pnas.org/lookup/suppl/doi:10.1073/pnas.1906365116/-DCSupplemental](http://www.pnas.org/lookup/suppl/doi:10.1073/pnas.1906365116/-DCSupplemental).

Published online July 10, 2019.

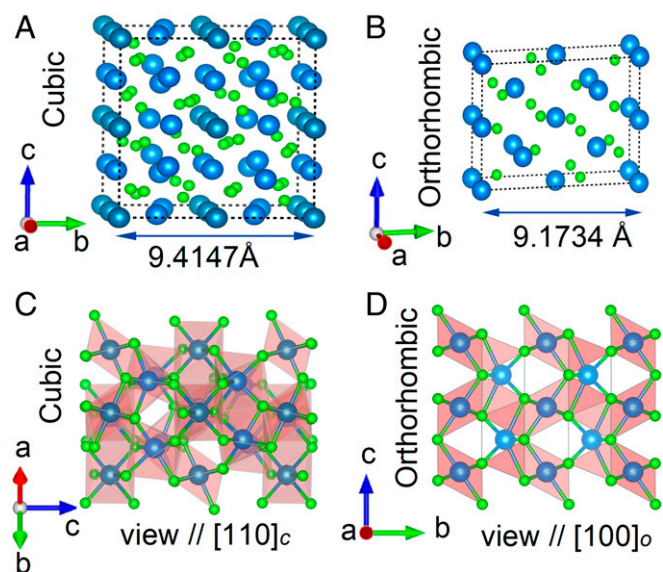


**Fig. 1.** Crystal structures of  $\text{Mn}_2\text{O}_3$ . The unit cell for (A) cubic and (B) orthorhombic pPv phase. (C) A view from  $[110]_c$  direction for cubic structure. (D) A view from a axis for orthorhombic structure. The low-pressure cubic phase and high-pressure orthorhombic phase show structure similarity indicating the potential for a martensitic phase transition.

(20, 30–33), and investigated the texture and lattice strain evolution in situ as well. The phase transitions in sesquioxide compounds ( $\text{M}_2\text{O}_3$ ,  $\text{M} = \text{Fe}, \text{Mn}, \text{Al}, \text{Cr}, \text{Tl}, \text{In}$ , etc.) are of great interest for materials science because of unique physical properties (34) as well as for geophysics due to the relevance

of their high-pressure structures to deep Earth minerals (35). Crystallized in a C-type rare-earth structure ( $\alpha\text{-Mn}_2\text{O}_3$ , space group  $Ia\bar{3}$ , mineral bixbyite) at ambient conditions, a direct transition to the postperovskite (pPv) structure ( $\delta\text{-Mn}_2\text{O}_3$ , space group  $\text{Cmcm}$ ) has been observed above 27 GPa (36, 37). Cubic bixbyite consists of alternating layers of less distorted and more distorted octahedra, while the crystal structure of the pPv phase consists of alternating layers of octahedral and bicapped trigonal prisms (Fig. 1). This could explain why  $\text{Mn}_2\text{O}_3$  transformed into a pPv type directly under high pressure instead of following the phase transitions found in other sesquioxide minerals (36) and also suggests a martensitic nature of this phase transition. Cubic  $\alpha\text{-Mn}_2\text{O}_3$  is a highly symmetric structure, while the high-pressure pPv phase is in a lower-symmetry orthorhombic structure, which makes it a good example to investigate variant selection under stress.

## Results and Discussion

We deformed the sample of  $\text{Mn}_2\text{O}_3$  powder in a DAC in compression from ambient pressure to 51.5 GPa at room temperature and observed the texture evolution through the phase transition in situ using r-DAC XRD (SI Appendix, Fig. S1). Platinum was used as a pressure calibrant. Diffraction data were analyzed with the Rietveld refinement method (38) as implemented in the software package MAUD (39). Fig. 2 shows unrolled diffraction images of  $\text{Mn}_2\text{O}_3$  at various pressures. The curved shape of the diffraction peak position as a function of azimuth represents the crystal lattice strain and is caused by the compressive stress generated in the nonhydrostatic environment. The systematic peak intensity variation with azimuth reflects the lattice preferred orientation (texture) of the phases in the sample. At low pressure there is a pure cubic phase with large lattice strain and strong texture appearing at 10.3 GPa (Fig. 2A and B). At 24.1 GPa, several extra diffraction peaks (represented by red

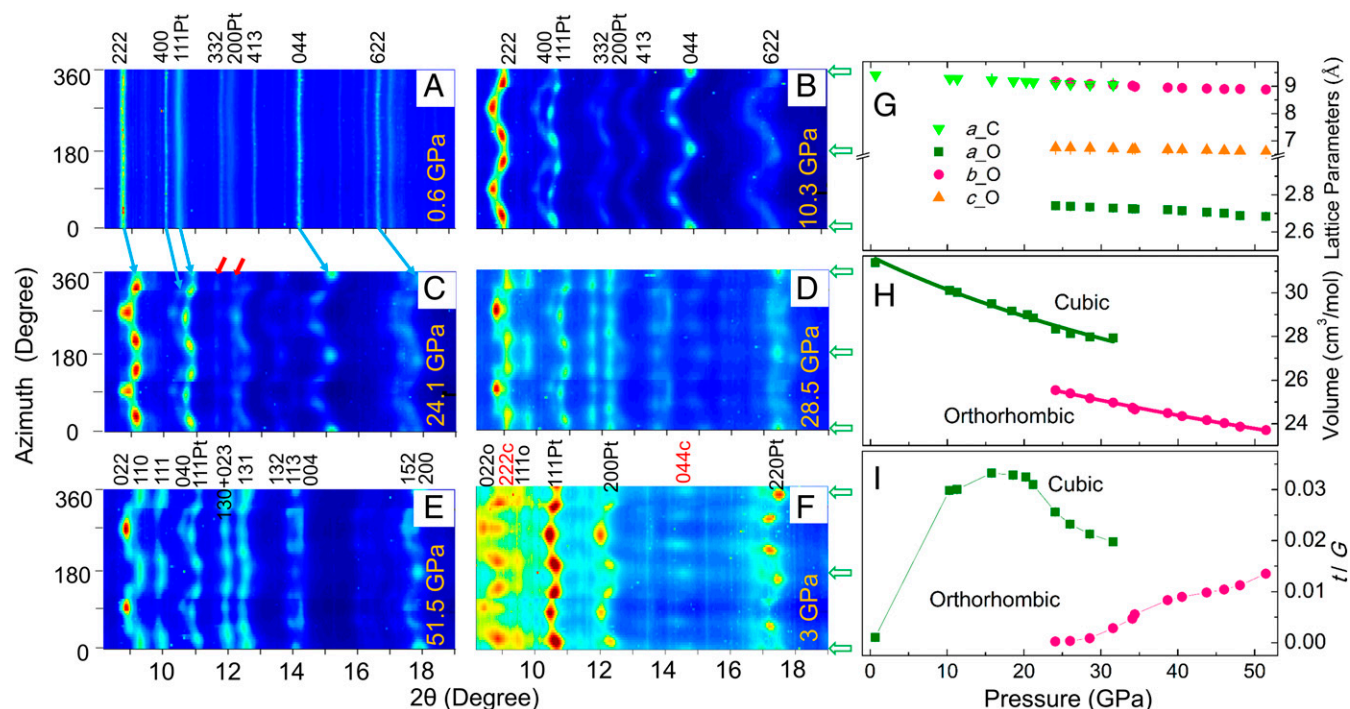


**Fig. 2.** Unrolled diffraction patterns and refinement results of  $\text{Mn}_2\text{O}_3$  under pressure. (A and B) cubic; (C and D) two phases mixture; (E) orthorhombic phase; (F) two phases mixture during decompression. Some diffraction peaks for the cubic phase, orthorhombic phase, and Pt are labeled. Red arrows in C indicate peaks for the high-pressure phase. Green arrows on the right side indicate the compression direction. Unit cell parameters (G) and molar volume (H) of cubic and orthorhombic-type  $\text{Mn}_2\text{O}_3$  under pressure. The dashed lines fit of the Birch–Murnaghan equation of state with  $K'_0$  fixed to be 4. (I)  $t/G$  as a function of pressure. The low initial  $t/G$  value of orthorhombic phase is a consequence of the large volume collapse during the phase transition.

arrows, Fig. 2C) appear, indicating the start of the phase transition. The high-pressure peaks initially show no lattice strain (straight lines) and then the strain increases with pressure, as shown in Fig. 2D at 28.5 GPa. Peaks of the low-pressure phase remain to 31.6 GPa, after which the phase transition is complete. This is consistent with the results reported by Yamanaka et al. (40) and Santillán et al. (36). The pressure was then continuously increased to 51.5 GPa, but no significant changes of diffraction patterns were observed (Fig. 2E). After decompression, the quenched sample returned to the low-pressure cubic phase with the same original lattice preferred orientation, indicating that this phase transformation is reversible (Fig. 2F).

Lattice parameters and lattice strain of both cubic and orthorhombic structures were extracted from the refinement results (Fig. 2 G–I). The lattice parameters and volume of the low-pressure phase in our measurement are comparable with Yamanaka et al. (40) and a bit higher than that of Santillán et al. (36). This difference might be caused by different pressure media. In the latter work, Ar was used as a pressure medium, whereas the former used a methanol–ethanol mixture and we used no pressure medium. The same effect has also been observed in  $\text{HoVO}_4$  (41) and  $\text{SmVO}_4$  (42), where lattice parameters are larger and also showed more obvious scatter when the experimental conditions induced large deviatoric stresses.

The molar volume decreases by 10% across the phase transition between 24.1 and 31.6 GPa (Fig. 2H). A large pressure-induced volume collapse from 10 to 22% has previously been reported in transition-metal compounds like  $\text{Fe}_3\text{O}_4$  (43),  $\text{Fe}_2\text{O}_3$  (44), and  $\text{MnS}_2$  (45). Both experiments and calculations have proved that the volume collapse is driven by a spin-state transition. At high pressure a high spin state is unstable compared with the low spin state.  $\alpha\text{-Mn}_2\text{O}_3$  displays a high spin state as estimated by calculations (46) and neutron diffraction (47, 48). Therefore, it is reasonable to suggest that the large volume collapse in  $\text{Mn}_2\text{O}_3$  during the phase transition is caused by the spin-state change under high pressure.

Fig. 2I displays the stress-bulk modulus ratio  $t/G$  as a function of pressure for both the cubic and pV phases of  $\text{Mn}_2\text{O}_3$ . This value representing the average lattice strain was obtained using the Triaxial Stress Isotropic E strain model implemented in MAUD and used for a first evaluation of the stress level in plastically deforming aggregates (32). In addition, the stress was also estimated from the platinum foil according to previous reports (49, 50). In the cubic phase, the  $t/G$  value first increases strongly with pressure and then remains almost stable in a range of pressure between 15.8 and 21.8 GPa, before it begins to decrease with the appearance of the high-pressure phase. This decrease might imply that grains with higher strain transformed to orthorhombic phase first. Also, in r-DAC experiments there are stress gradients between the center and the periphery of the sample. In the high-pressure phase, the initial lattice strain is almost zero but then it increases slowly with pressure. The much smaller lattice strain of the high-pressure phase compared with the C-type phase have also been observed in the unrolled diffraction patterns. In the two-phase mixture state (Fig. 2 C and D), it is quite clear that for the pV phase diffraction peak positions show minimal dependence on the azimuthal angle compared with those of the low-pressure phase. There is almost no lattice strain in the high-pressure phase at the beginning of the phase transition. The large volume collapse during the phase transition could be responsible for this lattice strain release and also causes the lattice strain of the low-pressure cubic phase to decrease.

The preferred orientation distributions were calculated by imposing axial symmetry about the compression direction. Inverse pole figures (IPFs), which describe the orientation of the compression axis relative to crystal coordinates, were obtained for both phases of  $\text{Mn}_2\text{O}_3$  (Fig. 3A). Pole densities are

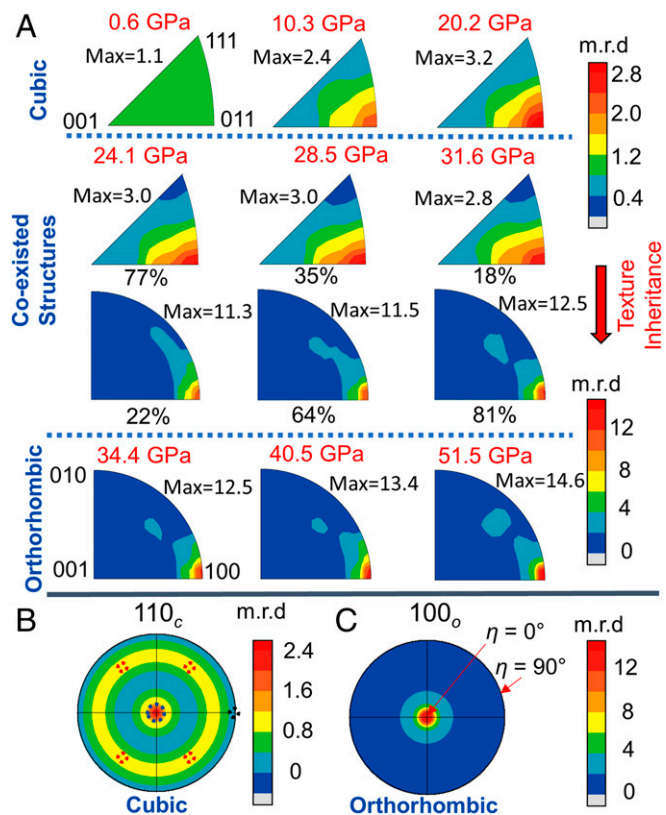


**Fig. 3.** Orientation relationship and variant selection during phase transition of  $\text{Mn}_2\text{O}_3$ . (A) Texture development under pressure/stress. IPFs of the compression direction showing the texture evolution of  $\text{Mn}_2\text{O}_3$  up to 51.5 GPa through the phase transition from the cubic to the orthorhombic structure. For each case, the experimental pressure values and the maximum pole densities are shown. The phase proportions of each phase during the phase mixture state are also indicated. Selected PFs of (B) cubic and (C) orthorhombic  $\text{Mn}_2\text{O}_3$  at 24.1 GPa.  $\eta = 0^\circ$  indicates the compression direction. Dashed circles in B show poles of 6 cubic  $\{110\}$  planes in a projection along the compression axis. Pole densities are expressed in m.r.d. Equal area projection.

represented in multiples of a random distribution (m.r.d.), where 1 m.r.d. corresponds to no preferred orientation. The starting material (0.6 GPa) was initially randomly oriented. Above 10.3 GPa ( $t/G = 0.0298$ ,  $t \sim 2$  GPa) the low-pressure cubic phase displayed a 110 texture, the strength increasing with pressure (and stress) and reaching its largest value of 3.2 m.r.d. at about 20.2 GPa ( $t/G = 0.0325$ ,  $t \sim 3.5$  GPa). This 110 texture is a typical compression texture for fcc metals that deform by  $\{111\}\langle 110 \rangle$  slip (51). Above the phase transition (24.1 GPa,  $t \sim 4$  GPa), the strength of the 110 texture began to decrease while the high-pressure phase developed a very strong texture at 100 with an intensity of 11.3 m.r.d. At this pressure, the average lattice strain of the cubic phase decreased to 0.026, while the orthorhombic phase displayed a much smaller lattice strain of about 0.0003 due to the phase transition and consequent volume collapse. The 100 texture became slightly stronger with further compression, increasing to 14.6 m.r.d. at 51.5 GPa ( $t/G = 0.0135$ ,  $t \sim 5.5$  GPa). The texture change during the phase transition suggests a relationship of  $\{110\}_c // (100)_o$ , where  $\{110\}_c$  are the lattice planes perpendicular to the stress direction. From unrolled diffraction images (Fig. 2A), it can be seen that during the phase transition, diffraction peak (400) of the cubic phase transferred to (040) of the orthorhombic phase, suggesting a relationship of  $\langle 100 \rangle_c // [010]_o$ . These two parallel relationships define the full orientation relation across the phase transition, although there might be some ambiguity due to the axial symmetry of the compression

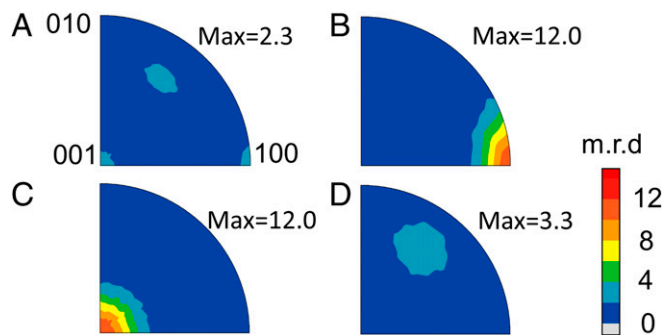


**Fig. 4.** Orientation distribution of orthorhombic  $\text{Mn}_2\text{O}_3$  obtained via modeling. There are three distinct types of IPFs of the compression direction: (A) IPF for the sum of all six variants (B) type I, (C) type II, (D) type III, corresponding to cubic  $\{110\}$  planes shown in blue, black, and red in Fig. 3B, respectively. The starting cubic  $\text{Mn}_2\text{O}_3$  fiber texture used for modeling is shown in *SI Appendix*, Fig. S6.

experiment. The texture we obtained here for the pPv phase is quite different from that reported for  $\text{Mn}_2\text{O}_3$  experiments using Ar as a pressure medium (36). In that work, the pPv phase showed a weak lattice preferred orientation of the (010) plane perpendicular to the loading axis of the DAC, which changed to (100) and (110) after annealing. It should be noted that an axial DAC geometry was used in that study, which is not ideal for the investigation of textures.

The preferred orientation in both cubic and orthorhombic phases can be compared with pole figures (PFs) (Fig. 3B and C) projected along the compression direction. They have axial symmetry to conform to the geometry of the deformation experiment. For cubic 110, two maxima are observed: one parallel to the compression direction at  $\eta = 0^\circ$  and a weaker concentration at  $\eta \sim 60^\circ$ . It is clear that only one  $\{110\}$  plane is in the center (compression direction) while four planes are at around  $60^\circ$  and one at  $90^\circ$ . For the orthorhombic phase (Fig. 3C), there is only one maximum at the center of the 100 PF, indicating all  $(100)_o$  lattice planes are preferentially oriented perpendicular to the compression direction. Due to the multiplicity of cubic symmetry, pole densities are never as strong as single symmetry directions such as  $[100]$  in orthorhombic. Based on the orientation relationship  $\{110\}_c // (100)_o$ , all  $\{110\}_c$  planes have the chance to become  $(100)_o$ . But, with stress there is obviously a variant selection and the orthorhombic phase selects one of the cubic  $\{110\}$  planes that is closest to perpendicular to the compression direction (Fig. 3B). Since the texture of the orthorhombic phase did not change much during further compression, the effect of plastic deformation on its texture can be excluded.

To quantitatively assess variant selection, we reviewed all possible variants associated with the cubic-to-orthorhombic transformation (Fig. 3B) in  $\text{Mn}_2\text{O}_3$  by following the symmetry of the parent cubic phase and orientation relationship  $\{110\}_c \langle 001 \rangle_c // (100)_o \langle 010 \rangle_o$ . Each of them was modeled by applying the corresponding rotation matrix with proper orthorhombic

crystal symmetry to different symmetry equivalent variants of the cubic orientation distribution functions at 20.2 GPa displayed in Fig. 3A. Resulting orientation distributions are characterized by three different types of IPFs as shown in Fig. 4. If there is no variant selection during the phase transformation, then the IPF of the compression direction for orthorhombic  $\text{Mn}_2\text{O}_3$  has three maxima, type I, type II, and type III, and the overall texture strength is fairly weak (Fig. 4A). In the type-I IPFs (100) planes are oriented approximately normal to the compression direction (Fig. 4B) and this is most consistent with the experimental results (Fig. 3A and C). It corresponds to the cubic (110) plane in the center of the PF as indicated by a blue circle in Fig. 3B. For type II, which is relevant to the (110) plane shown by the black circle in Fig. 3B, (001) planes are oriented approximately normal to the compression direction (Fig. 4C). The type-III IPF in Fig. 4D (corresponding to cubic  $\{110\}$  planes shown in red in Fig. 3B) has a maximum indicating that planes with Miller indices close to  $\{153\}$  are oriented approximately normal to the compression direction.

Our study provides an example of almost-perfect variant selection during a phase transition under stress. For  $\text{Mn}_2\text{O}_3$ , the cubic  $\{110\}$  and orthorhombic (100) lattice planes have many similarities in atomic arrangements as clearly shown in Fig. 1C and D. Viewed along  $[110]_c$ , the cubic phase consists of alternating layers of less distorted and more distorted octahedra. In the orthorhombic phase, the volume collapse associated with the transition produces a more compact arrangement with alternating layers of octahedral and bicapped trigonal prisms along  $[100]_o$ . This explains the texture transfer of  $(110)_c$  to  $(100)_o$  during the phase transition. In addition, the axial stress applied in our experiments will lead to stronger strain of lattice planes perpendicular to the compression direction than others. Thus, these planes will more easily transfer to the high-pressure phase and consequently result in the variant selection during the phase transition.

## Materials and Methods

$\text{Mn}_2\text{O}_3$  powder was purchased from Sigma-Aldrich. The high-pressure r-XRD was conducted at BL10XU of Spring 8, Japan. A panoramic-type DAC with large openings was used to allow r-XRD (*SI Appendix*, Fig. S1). The sample was ground into fine powder and loaded in an X-ray-transparent boron-epoxy gasket with a hole drilled at the center and inserted into a kapton support. A small fragment of  $\sim 10\text{-}\mu\text{m}$ -thick platinum foil was added on top of the sample and was used as a pressure calibrant in each experiment. The deviatoric stress on the sample was maximized by using no pressure medium. A monochromatic X-ray of wavelength 0.4142 Å was collimated to a beam size of  $30\ \mu\text{m} \times 30\ \mu\text{m}$  and focused onto the sample. An imaging plate area detector (Rigaku Co.) was used to collect XRD images. Instrument parameters, such as sample-to-detector distance, beam center, and detector tilt, were calibrated using a  $\text{CeO}_2$  standard before the experiment. The experiment was carried out at room temperature. More details about data analysis and modeling can be found in *SI Appendix*.

**ACKNOWLEDGMENTS.** We acknowledge the support of National Science Associated Funding (Grant U1530402). H.-R.W. is appreciative for support from NSF (EAR-1343908) and Department of Energy (DE-FG02-05ER15637). The synchrotron radiation experiments were performed at the BL10XU of SPring-8 with the approval of the Japan Synchrotron Radiation Research Institute (JASRI) (Proposals 2014B1254, 2017A1302).

1. L. Kaufman, M. Cohen, Thermodynamics and kinetics of martensitic transformations. *Prog. Met. Phys.* **7**, 165–246 (1958).
2. E. C. Bain, N. Dunkirk, The nature of martensite. *Trans. AIME* **70**, 25–47 (1924).
3. J. W. Christian, *The Theory of Transformations in Metals and Alloys* (Pergamon, 2002).
4. V. Podzorov, B. G. Kim, V. Kiryukhin, M. E. Gershenson, S. W. Cheong, Martensitic accommodation strain and the metal-insulator transition in manganites. *Phys. Rev. B* **64**, 140406 (2001).
5. J. Zhang, C. C. Tasan, M. J. Lai, A. C. Dippel, D. Raabe, Complexion-mediated martensitic phase transformation in Titanium. *Nat. Commun.* **8**, 14210 (2017).
6. X. Moya et al., Giant electrocaloric strength in single-crystal  $\text{BaTiO}_3$ . *Adv. Mater.* **25**, 1360–1365 (2013).
7. Y. Tian et al., Ultrahard nanotwinned cubic boron nitride. *Nature* **493**, 385–388 (2013).
8. L. Zhang et al., Amorphous martensite in  $\beta$ -Ti alloys. *Nat. Commun.* **9**, 506 (2018).
9. Y. Ogawa, D. Ando, Y. Souto, J. Koike, A lightweight shape-memory magnesium alloy. *Science* **353**, 368–370 (2016).
10. J. Zhang et al., A nanoscale shape memory oxide. *Nat. Commun.* **4**, 2768 (2013).
11. K. Otsuka, X. Ren, Physical metallurgy of Ti–Ni-based shape memory alloys. *Prog. Mater. Sci.* **50**, 511–678 (2005).
12. P. Castany, Y. Yang, E. Bertrand, T. Gloriant, Reversion of a parent  $\{332\}(113)_\beta$  martensitic twinning system at the origin of  $\{332\}(113)_\beta$  twins observed in metastable  $\beta$  titanium alloys. *Phys. Rev. Lett.* **117**, 245501 (2016).
13. V. I. Levitas, A. M. Roy, Multiphase phase field theory for temperature- and stress-induced phase transformations. *Phys. Rev. B* **91**, 174109 (2015).
14. Z. Nishiyama, X-ray investigation of the mechanism of the transformation from face centered cubic lattice to body centered cubic. *Sci. Rep. Tohoku Univ.* **23**, 637–664 (1934).

15. G. Kurdjumov, G. Sachs, Over the mechanisms of steel hardening. *Z. Phys.* **64**, 325–343 (1930).
16. W. G. Burgers, On the process of transition of the cubic-body-centered modification into the hexagonal-close-packed modification of zirconium. *Physica* **1**, 561–586 (1934).
17. R. K. Ray, J. J. Jonas, Transformation textures in steels. *Int. Mater. Rev.* **35**, 1–36 (1990).
18. P. Bate, B. Hutchinson, The effect of elastic interactions between displacive transformations on textures in steels. *Acta Mater.* **48**, 3183–3192 (2000).
19. H. Beladi, Q. Chao, G. S. Rohrer, Variant selection and intervariant crystallographic planes distribution in martensite in a Ti–6Al–4V alloy. *Acta Mater.* **80**, 478–489 (2014).
20. H. R. Wenk, P. Kaercher, W. Kanitpanyacharoen, E. Zepeda-Alarcon, Y. Wang, Orientation relations during the  $\alpha$ - $\omega$  phase transition of zirconium: In situ texture observations at high pressure and temperature. *Phys. Rev. Lett.* **111**, 195701 (2013).
21. S. Merkel, H.-R. Wenk, P. Gillet, H.-k. Mao, R. J. Hemley, Deformation of polycrystalline iron up to 30 GPa and 1000 K. *Phys. Earth Planet. Inter.* **145**, 239–251 (2004).
22. L. Miyagi *et al.*, In situ phase transformation and deformation of iron at high pressure and temperature. *J. Appl. Phys.* **104**, 103510 (2008).
23. S. Merkel, H. P. Liermann, L. Miyagi, H. R. Wenk, In situ radial X-ray diffraction study of texture and stress during phase transformations in bcc-, fcc- and hcp-iron up to 36 GPa and 1000 K. *Acta Mater.* **61**, 5144–5151 (2013).
24. P. Kaercher, S. Speziale, L. Miyagi, W. Kanitpanyacharoen, H.-R. Wenk, Crystallographic preferred orientation in wüstite (FeO) through the cubic-to-rhombohedral phase transition. *Phys. Chem. Miner.* **39**, 613–626 (2012).
25. D. P. Dobson *et al.*, Strong inheritance of texture between perovskite and post-perovskite in the D' layer. *Nat. Geosci.* **6**, 575–578 (2013).
26. X. M. Zeng, A. Lai, C. L. Gan, C. A. Schuh, Crystal orientation dependence of the stress-induced martensitic transformation in zirconia-based shape memory ceramics. *Acta Mater.* **116**, 124–135 (2016).
27. X. M. Zeng *et al.*, In-situ studies on martensitic transformation and high-temperature shape memory in small volume zirconia. *Acta Mater.* **134**, 257–266 (2017).
28. M. Mamivand, M. Asle Zaeem, H. El Kadiri, Shape memory effect and pseudoelasticity behavior in tetragonal zirconia polycrystals: A phase field study. *Int. J. Plast.* **60**, 71–86 (2014).
29. M. Mamivand, M. Asle Zaeem, H. El Kadiri, Phase field modeling of stress-induced tetragonal-to-monoclinic transformation in zirconia and its effect on transformation toughening. *Acta Mater.* **64**, 208–219 (2014).
30. S. Merkel *et al.*, Deformation of (Mg,Fe)SiO<sub>3</sub> post-perovskite and D' anisotropy. *Science* **316**, 1729–1732 (2007).
31. L. Miyagi, W. Kanitpanyacharoen, P. Kaercher, K. K. Lee, H. R. Wenk, Slip systems in MgSiO<sub>3</sub> post-perovskite: Implications for D' anisotropy. *Science* **329**, 1639–1641 (2010).
32. B. Yue *et al.*, Deformation behavior across the zircon-scheelite phase transition. *Phys. Rev. Lett.* **117**, 135701 (2016).
33. B. Chen *et al.*, Detecting grain rotation at the nanoscale. *Proc. Natl. Acad. Sci. U.S.A.* **111**, 3350–3353 (2014).
34. O. Gomis *et al.*, High-pressure structural and elastic properties of Ti<sub>2</sub>O<sub>3</sub>. *J. Appl. Phys.* **116**, 133521 (2014).
35. T. S. Duffy, Some recent advances in understanding the mineralogy of Earth's deep mantle. *Philos. Trans. A Math. Phys. Eng. Sci.* **366**, 4273–4293 (2008).
36. J. Santillán, S. H. Shim, G. Shen, V. B. Prakapenka, High-pressure phase transition in Mn<sub>2</sub>O<sub>3</sub>: Application for the crystal structure and preferred orientation of the CaIrO<sub>3</sub> type. *Geophys. Res. Lett.* **33**, L15307 (2006).
37. S. H. Shim, D. LaBounty, T. S. Duffy, Raman spectra of bixbyite, Mn<sub>2</sub>O<sub>3</sub>, up to 40 GPa. *Phys. Chem. Miner.* **38**, 685–691 (2011).
38. H. M. Rietveld, A profile refinement method for nuclear and magnetic structures. *J. Appl. Cryst.* **2**, 65–71 (1969).
39. H. R. Wenk *et al.*, Rietveld texture analysis from synchrotron diffraction images. II. Complex multiphase materials and diamond anvil cell experiments. *Powder Diffr.* **29**, 220–232 (2014).
40. T. Yamanaka, T. Nagai, T. Okada, T. Fukuda, Structure change of Mn<sub>2</sub>O<sub>3</sub> under high pressure and pressure-induced transition. *Z. Kristallogr.* **220**, 938–945 (2005).
41. A. B. Garg *et al.*, High-pressure structural behaviour of HoVO<sub>4</sub>: Combined XRD experiments and ab initio calculations. *J. Phys. Condens. Matter* **26**, 265402 (2014).
42. C. Popescu *et al.*, Pressure-induced phase transformation in zircon-type orthovanadate SmVO<sub>4</sub> from experiment and theory. *J. Phys. Condens. Matter* **28**, 035402 (2016).
43. S. Ju, T. Y. Cai, H. S. Lu, C. D. Gong, Pressure-induced crystal structure and spin-state transitions in magnetite (Fe<sub>3</sub>O<sub>4</sub>). *J. Am. Chem. Soc.* **134**, 13780–13786 (2012).
44. J. Badro *et al.*, Nature of the high-pressure transition in Fe<sub>2</sub>O<sub>3</sub> hematite. *Phys. Rev. Lett.* **89**, 205504 (2002).
45. S. A. J. Kimber *et al.*, Giant pressure-induced volume collapse in the pyrite mineral MnS<sub>2</sub>. *Proc. Natl. Acad. Sci. U.S.A.* **111**, 5106–5110 (2014).
46. C. Franchini, R. Podloucky, J. Paier, M. Marsman, G. Kresse, Ground-state properties of multivalent manganese oxides: Density functional and hybrid density functional calculations. *Phys. Rev. B* **75**, 195128 (2007).
47. M. Reguiski, R. Przenioslo, I. Sosnowska, D. Hohlwein, R. Schneider, Neutron diffraction study of the magnetic structure of  $\alpha$ -Mn<sub>2</sub>O<sub>3</sub>. *J. Alloys Compd.* **362**, 236–240 (2004).
48. E. Cockayne, I. Levin, H. Wu, A. Llobet, Magnetic structure of bixbyite  $\alpha$ -Mn<sub>2</sub>O<sub>3</sub>: A combined DFT+U and neutron diffraction study. *Phys. Rev. B* **87**, 184413 (2013).
49. S. M. Dorfman, S. R. Shieh, T. S. Duffy, Strength and texture of Pt compressed to 63 GPa. *J. Appl. Phys.* **117**, 065901 (2015).
50. A. K. Singh *et al.*, Strength of polycrystalline coarse-grained platinum to 330 GPa and of nanocrystalline platinum to 70 GPa from high-pressure x-ray diffraction data. *J. Appl. Phys.* **103**, 063524 (2008).
51. A. D. Rollett, S. I. Wright, "Typical textures in metals," in *Texture and Anisotropy Preferred Orientations in Polycrystals and Their Effect on Materials Properties*, U. F. Kocks, C. N. Tomé, H. R. Wenk, Eds. (Cambridge University Press, 2000).